Charge transport through functionalized graphene quantum dots embedded in a polyaniline matrix

Charge transport through functionalized graphene quantum dots embedded in polyaniline matrix

Abu Bakar Siddique[1, 2], Kelly Morrison[3], Guru Venkat [3, 4], Ashit Kumar Pramanik[5], Niladri Banerjee[3], and Mallar Ray[6*]

[1] *Department of Electronics and Communication Engineering, Aditya College of Engineering and Technology, Surampalem -533437. East Godavari, Andhra Pradesh, India.*

[2] *Dr. M. N. Dastur School of Materials Sciences and Engineering, IIEST, Shibpur, Botanic Garden, Howrah 711103, India*

[3] *Department of Physics, Loughborough University, Loughborough, LE11 3TU, United Kingdom*

[4] *Department of Materials Science & Engineering, University of Sheffield, Sheffield, S10 2TN, United Kingdom*

[5] *National Metallurgical Laboratory, Jamshedpur, 831007, Jharkhand, India*

[6] *School of Engineering and Sciences, Tecnológico de Monterrey, Monterrey, 64849, Nuevo Leon, Mexico*

*E-mail: mallar.ray@tec.mx

Abstract

Nitrogen-functionalized graphene quantum dots embedded in polyaniline matrix (NGQD-PANI) are extremely promising candidates for the development of next-generation sensors and

for thermoelectric materials design with the distinct advantage of tunability of electronic properties by controlled doping and/or by controlling the inherent disorder in the microstructure. While their application is increasing in photovoltaics, energy storage and sensing technologies, a clear understanding of conduction in these hybrid systems is lacking. Here, we report a comprehensive study of NGQD-PANI composites with varying NGQD doping levels over a wide range of temperature. We show distinct regimes of conduction as a function of temperature which include: a transition from Efros-Shklovskii and Larkin-Khmelnitskii variable range hopping at low temperatures to thermally driven electron transport at higher temperatures. Importantly, we find a remarkable 50-fold enhancement in conductivity for 10% NGQD doped samples and tunability of the crossover temperature between different regimes as a function of the applied voltage bias and doping. Our work provides a general framework to understand the interplay of extrinsic parameters like temperature and voltage bias with intrinsic material properties like doping which drives the electronic properties in these hybrid systems of technological importance.

Keywords: graphene quantum dots, polyaniline, nanocomposite, electrical transport, variable range hopping, activated conduction

Introduction

Electrical transport characteristics of graphene quantum dots (GQDs) represent remarkable characteristics including excited states in bilayer dots,[1] formation of gate-tuneable Andreev bound states in proximity to superconductors,[2] and periodic and nonperiodic Coulomb blockade peaks.[3-4] Most of these transport studies have been carried out on GQDs that are either grown epitaxially or transferred to some device architecture fabricated on SiO_2 or boron nitride substrates. While these studies are important for fundamental understanding and for the development of GQD based electronic devices, a parallel scalable approach for sensor and thermoelectric materials design is worthwhile as it utilizes the exotic properties of GQDs embedded in a matrix. This approach forms a bulk nanocomposite where the overall properties are controlled by the nanoscale constituents, the background matrix and their interaction. Such systems offer conductivity tunability from an insulator to a metal by simply varying the doping and the inherent disorder in the microstructure and is often an advantage in applications such as thermoelectric devices.[5] Conducting polyaniline (PANI) offers an excellent choice as a matrix material due to the remarkable properties it possesses — extended π-conjugated system, optical transparency, mechanical stability, ease of the synthesis, an inexpensive monomer, and most importantly, easy tunability of the electrical property through doping.[6-7]

Consequently, GQD-PANI nanocomposite systems have attracted significant attention. Different types of GQD-PANI composites have been developed and investigated for their potential applications in sensing,[8-9] photovoltaics,[10-12] and energy-storage devices (supercapacitors and pseudocapacitors).[13-14] For these applications, a rigorous understanding of their transport properties is essential. A key ingredient in understanding the charge transport mechanism in these quasi-1D flexible and conducting polymers is to recognise the strong electron-lattice interactions.[15] Electrical conductivity of conjugated polymers is therefore

understood in terms of coupled, self-localized, non-linear excitations - solitons, polarons and bipolarons.[16] A distinguishing feature of PANI from other conducting polymers is the lack of degenerate ground states. This means that the conventional models in polymers with degenerate ground states involving topological solitons cannot be applied for PANI.[17] Consequently, polarons and/or bipolarons have been extensively used to understand electrical conduction,[18] since their existence does not require a strict degeneracy of the ground state configurations. While this polaron/bipolaron framework has its own complexities depending on the types of electron-phonon interactions, here our primary aim is to understand the mechanism of conduction of the charge carriers without worrying about the mechanism of their formation.

Past studies have reported hysteresis and non-linearity in *I-V* characteristics for GQD-PANI composites which is usually attributed to surface or edge-related states acting as charge trapping centres.[19-20] Charge transport in graphene oxide-dots and carbon micro-spheres in a PANI matrix[21-22] has also been reported where the dominant mechanism is three dimensional variable-range hopping. Similar studies in other composite systems like 0D carbon stabilized in poly-4-styrene sulphonate found nearly linear *I-V* followed by current saturation at low bias resulting from C–C sp^2 hybridization.[23] However, to the best of our knowledge there is no comprehensive study about the charge transport in GQD-PANI composites operating over a wide temperature range which can provide us with key insights into the charge transport mechanisms and help in developing strategies to tune the conductivities of these nanocomposite systems.

To develop a general framework for understanding charge transport, we studied the *I-V* characteristics of nitrogen functionalized GQDs (NGQDs) dispersed in PANI over a temperature range varying from 70 to 300 K. In this study, the N-functionalized samples were preferred over other variants of GQDs since, N-doped carbon nanomaterials have been reported

to favourably facilitate charge transfer, storage and interaction, higher electrical conductivity and better surface hydrophilicity.[24] Conduction in N-GQD is reported to be mediated via exponentially distributed trap states which lead to enhanced storage capacity.[25] For enhanced conduction in PANI composites we would like to generate more free holes since the conduction through PANI network is dictated by p-type polaronic defect states. NGQDs, therefore provide a better alternative to other variants of GQDs, as coupling of delocalized π-electrons of NGQDs with polarons in PANI should facilitate generation of free holes. Additionally, it has also been recently reported that presence of abundant N sites in N-GQDs facilitate interfactial charge transfer and participate in the crystallization of perovskite film.[26] All these features of NGQDs prompted us to choose NGQDs as the dopant. Our results indicate that the inclusion of NGQDs in a PANI matrix significantly alters the *I-V* characteristics of bare PANI – the dynamic conductivity and storage capacity of the composite increase and the *I-V* characteristics exhibit hysteresis. Strikingly, we find that the electrical transport in the system is not constant over the whole temperature range and we clearly identify temperature, composition and bias-dependent regimes dominated by distinctly different charge transport mechanisms. The ability to precisely tune the electrical properties of NGQD-PANI composite systems by adjusting NGQD concentration, temperature and bias voltage, makes it an ideal system for a wide range of sensor and energy storage applications.

Experimental

Synthesis: NGQDs in aqueous dispersion were prepared by standard hydrothermal method discussed earlier.[27] Oxidized aniline was distilled 2-3 times and preserved for the in-situ synthesis of PANI-based composite.[28] For the development of NGQD-PANI composites, the constituents were taken in fixed molar ratios and the amount of NGQDs was varied with respect to aniline to form composites with varying concentrations of NGQDs. Briefly, an aliquot of 2.87 g of cetyl trimethyl ammonium bromide (CTAB) was added to 0.17 M aqueous solution of camphorsulfonic acid (CSA), followed by the addition of requisite amounts of NGQDs. CTAB was used as a surfactant. The solutions were stirred for 5 minutes and 4 g of purified aniline was added to these solutions and stirred for an additional 1 hour. Subsequently, 0.085 M ammonium persulfate (APS) solution was added drop wise to the above mixture. The mixed solutions were constantly stirred for one day to facilitate slow polymerization. Throughout the synthesis process the solutions were kept in an ice bath maintained at ~10°C. Finally, the black NGQD-PANI precipitate was washed with DI water and ethanol repeatedly in a microfiltration unit, until the filtrate became colourless. The filtrate was then dried under vacuum at 80˚C for 24 hours to obtain the NGQD-PANI nanocomposite powder. Nanocomposites corresponding to 0, 1, 5 and 10 percent of NGQDs with respect to aniline were prepared and the samples were named as S0, S1, S5 and S10, respectively. Approximately 200 mg powder of each sample were pressed for 10 minutes by applying 150 kg/cm^2 pressure in a 13 mm diameter die in a hydraulic press. The 13 mm diameter pellets, were used for electrical characterization.

Characterization: X-ray diffraction (XRD) studies were carried out by using a Brucker D8 advanced diffractometer using Cu $K_{\alpha 1}$ radiation. The distribution and microstructure were investigated by a JSM-7610F, JEOL field emission scanning electron microscope (FE-SEM) and a 200 kV, JEOL JEM-2200 FS high resolution transmission electron microscope (HR-TEM). We used a GATAN energy filtered (EF-) TEM for elemental mapping and for electron

energy loss spectroscopy (EELS) study. UV-visible spectroscopy was done by a JASCO V-750, UV-VIS spectrophotometer and Fourier transform infrared (FTIR) spectra were recorded by JACSO 4700 LE. A Keithley 2400 source meter was used to obtain the I-V measurements, where an I-V sweep was obtained between +10 and -10V with 2500 steps. Samples were wired in the 4-probe configuration, with a voltage lead separation of approximately 4 mm. The sample measurement puck was mounted onto a copper sample holder that was directly attached to the cold finger of a closed cycle cryogen free cryostat from Advanced Research Systems. The cold finger temperature was monitored by a Cernox sensor and at each set temperature, the system was left to equilibrate for a minimum of 10 minutes (with tolerance +/- 0.1K) before measurement. For I-V measurements the pellets were cut into $4 \times 3 \times 1.4$ mm^3 rectangular sized specimens which were mounted onto an 8-pin puck (copper pads) and contacted with copper wires using silver paint. The dimensions of all the samples for I-V measurements are tabulated in the supporting information Table S1.

Results and Discussions

Structural features:

The gross structural characteristics of the NGQDs and the NGQD-PANI composites are summarized in Figure 1. The HR-TEM image shown in Figure 1a reveals that the NGQDs are spherical and reasonably well-distributed in shape and size. The crystalline character of the dots is evident from the corresponding selected area electron diffraction pattern (SAEDP) shown in Figure 1b, which reveals a diffraction reinforced diffused ring like pattern due to (002) planes of randomly oriented graphene crystals.[29] The sizes of these crystalline dots vary between 1 and 7 nm, with a modal diameter of 2.5 nm [Figure 1c]. The size distribution histogram was constructed with sizes estimated from several TEM micrographs (see supporting information for more TEM images). The four panels in Figure 1d are the elemental maps of C

(red), N (green), O (blue) and their composite map obtained by EF-TEM measurements. In the top left panel we see a circular cluster of C atoms corresponding to the carbon core of a single GQD. The correspondence of this circular cluster with the HRTEM image of an NGQD is shown in the supporting information (Figure S2). It appears from the top right and the bottom left panels, denoting the N and O maps, respectively, that the N and O atoms are concentrated in zones close to the C atoms. From the composite image shown in the bottom right panel of Figure 1d, it becomes evident that N and O atoms cluster around the surface of the carbon dot, suggesting the attachment of the N in amines onto the GQDs.
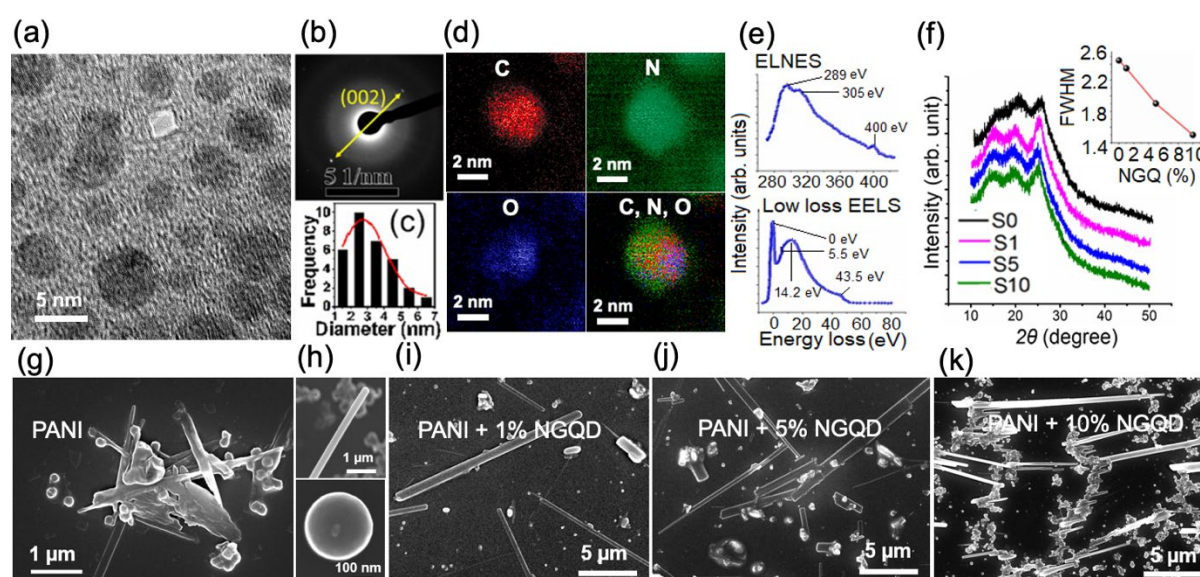

Figure 1. Structural features of the NGQD and NGQD-PANI composites: (a) bright field HR-TEM micrograph of the NGQDs, (b) SAEDP showing distinct signature of crystallinity, (c) the size distribution histogram, (d) elemental maps of C, N, O and the composite image obtained by EF-TEM measurements, showing the distribution of C, N and O in a single NGQD, (e) the EELS spectra showing the C-k edge energy loss near edge structure (top) the low energy loss spectrum (bottom), (f) XRD profiles of bare PANI (S0) and the NGQD-PANI composites (S1, S5 and S10); the variation of the FWHM of the XRD peak at $2\theta \sim 25^0$ is shown as inset, (g) SEM image of bare PANI having rod-like and agglomerated spherical structures, (h) shows

the magnified image of individual PANI structures – rod (top) and sphere (bottom), (i), (j) and (k) are the SEM micrographs of the PANI-NGQD composites – S1, S5 and S10, respectively.

The incorporation of nitrogen and the 2D nature of the dots are further illustrated in the carbon-K energy-loss near edge structure (ELNES) spectrum and the low-loss EELS spectrum of the NGQDs shown in Figure 1e. The peaks at 289 and 305 eV appearing in the ELNES spectrum can be assigned respectively to $1s{\rightarrow}\pi^*$ and $1s{\rightarrow}\sigma^*$ transitions in graphitic carbon, while the peak at 400 eV corresponds to $1s{\rightarrow}\pi^*$ transition of nitrogen. The positions of the $1s{\rightarrow}\pi^*$ and $1s{\rightarrow}\sigma^*$ peaks indicate a relatively higher energy loss compared to pure graphite, and is consistent with the findings reported for similar systems.[30] The low-loss EELS spectrum of the NGQDs shown in the bottom panel of Figure 1e, reveals peaks at 5.5 eV and 14.2 eV, corresponding to the π^* surface plasmon and $\pi^* + \sigma^*$ bulk plasmon, respectively and the positions of these peaks unambiguously indicate the formation of 2D graphene layers. In fact, the appearance of the $\pi^* + \sigma^*$ bulk plasmon peak at 14.2 eV is suggestive of single layer graphene,[31] although we will not focus on this in the current study. Finally, the hump peaking at 43.5 eV confirms the introduction of nitrogen in the graphene layer. Therefore, the results of HR-TEM and EELS firmly establish the formation of NGQDs.

The x-ray diffraction patterns of PANI and the NGQD-PANI shown in Figure 1f are dominated by features of PANI. The diffraction peak detected at 2θ ~15° can be attributed to the characteristic repeating benzenoid and quinoid units while the shoulder-like feature at ~20° corresponds to the periodicity in the direction parallel to the (020) planes of the PANI chains or rods. The feature centred at ~25° is due to the (200) planes perpendicular to the PANI chains.[32] A broad hump in the XRD pattern is expected to appear at 2θ ~25° due to the crystalline GQDs but this feature is masked by the broad PANI band appearing at the same 2θ value. Interestingly, the peaks corresponding to different planes of PANI become sharper with

the increase in the content of NGQD in the different composites. In fact, a plot of the FWHM of the peak centred at ~25° is found to decrease consistently with increase in NGQD concentration (inset, Figure 1f). This implies that crystallinity of PANI effectively increases with increase in NGQD as a consequence of the interaction of quinoid N-active sites of PANI with graphitized structure of NGQD resulting in conjugate bonding.[33]

Figures 1g-k are the SEM images of pelletized PANI and NGQD-PANI composites. The micrographs suggest that in-situ synthesis of PANI co-doped with CSA and NGQD produces a mixture of quasi-1D and spherical structures of PANI. The overall structure consists of non-aligned PANI rods with high aspect ratio (average ~27) along with some agglomerated lumps [Figure 1g]. Individual structures of quasi 1D, rod-like PANI and spherical PANI that constitute the randomly distributed agglomerates are shown in the higher magnification images in the top and bottom panels of Figure 1h, respectively. Since the sizes of NGQDs are very small (average diameter ~2.5 nm) compared to the PANI structures, it is impossible for SEM to simultaneously resolve PANI and NGQD in the same micrograph. The presence of a carbon backbone in both the structures along with the presence of nitrogen groups also inhibit the formation of distinct contrasts in electron microscopy. Interestingly, we note that with the increase in NGQDs from 1% to 10% in samples S1 to S10, there is a development of adjunction or interwinding in the morphology of the nanorods resulting in lesser agglomerated oligomers and more aligned PANI as evidenced from the micrographs shown in Figures 1i-k. This phenomenon becomes distinct for the sample S10 with 10% NGQD [Figure 1k]. The induction of interwinding and consequent alignment of the PANI nanorods can be attributed to the addition of NGQDs. This finding is in perfect agreement with the XRD results, which shows that the increase in percentage of NGQDs effectively increases the crystallinity resulting from the interaction between the graphitized NGQDs and the N-active sites of PANI.

The mechanism of formation of the NGQD-PANI composites is illustrated in the schematic shown in Figure 2a. The FTIR spectra of NGQD, PANI and the composites shown in Figure 2b, provide further support to the proposed mechanism. The signature peaks of NGQDs at 1376 and 1226 cm^{-1} corresponding to the bending vibration of C-NH,[34] and stretching vibration of C-N,[35] respectively, do not appear in the FTIR spectra of the NGQD-PANI composites, suggesting conjugate bonding of NGQDs with the repeating units of the aniline,[33] as indicated in the schematic, Figure 2a. It is highly unlikely that the absence of these signature peaks arise from a low concentration of pure NGQD after filtration as the slow polymerization technique adopted here ensures that nearly all of the reactants are utilized in the polymerization process and there is sufficient NGQD in the filtered sample. The absorption bands peaking at 1572 cm^{-1} and 1492 cm^{-1} are due to the stretching vibrations of C=N in quinoid and C=C in benzenoid, respectively.[36] Both these peaks become more intense with the increase in the NGQD, indicating bonding between aniline and NGQD. However, the ratio of the intensities of the peaks at 1572 cm^{-1} and 1492 cm^{-1} remains ~1:1, suggesting mixed oxidation state of PANI.[37] The peak appearing at 1300 cm^{-1} can be attributed to stretching vibration modes of C-N secondary aromatic amines and the one at 1238 cm^{-1} to C=N stretching vibration in a polaron structure. These two peaks also intensify with the increase in the NGQD concentration, signifying enhanced polaron structure. Similar enhancement of these polaronic peaks due to doping has been reported earlier in doped PANI systems with its origin linked to the enhanced conductivity.[38-39] The band detected at 1110 cm^{-1} for S10 may be ascribed to the polaron band vibration due to doping with the NGQDs.[40] With decrease in the NGQDs in samples from S10 to S0, this peak becomes less intense and shifts to 1150 cm^{-1} for S0 (PANI). This also qualitatively suggests that the increase in the NGQD concentration increases the polaron vibrations. The peak detected at 800 cm^{-1} is the out-of-plane bending mode of C-H of the 1,4-

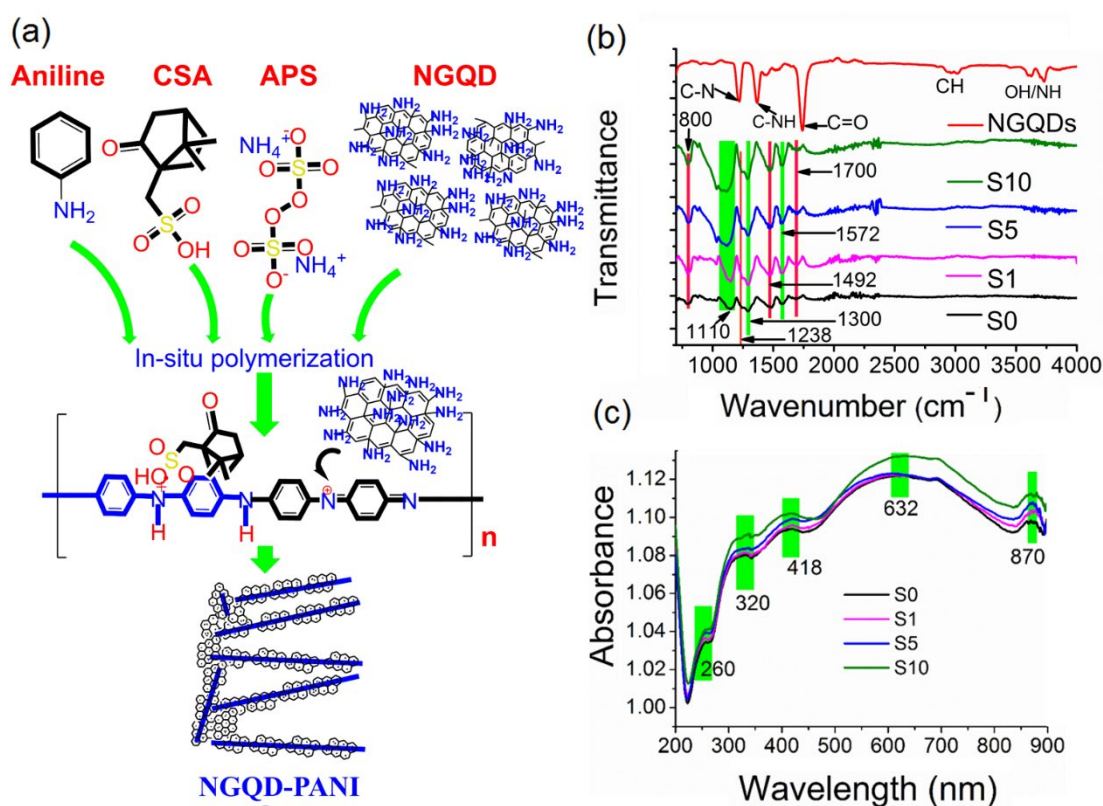disubstituted benzene ring, and the band at around 1700 cm^{-1} is the characteristic peak of CSA.[41]

Figure 2. Formation of NGQD-PANI composites. (a) a schematic illustrating the mechanism of formation of NGQD-PANI composites leading to interwind networks, (b) and (c) are respectively the FTIR and UV-visible spectra of NGQD, PANI and the composites (S1, S5 and S10).

The UV-vis absorption profiles of the NGQD-PANI composites shown in Figure 2c, are dominated by the absorption features of PANI. In all the absorption profiles we see five absorption bands peaking at 260 nm, 320 nm, 418 nm, 632 nm and 870 nm, respectively. The band at 260 nm is the characteristic benzenoid band,[42] whereas the one at 632 nm is due to quinoid segment.[43] The band peaking at 320 nm represents the reduced state, while the bands at 418 nm and 870 nm represent the oxidized states of the doped PANI.[44] These two oxidized states correspond to two different polaron transitions — the band at 418 nm for the π*-polaron

12

and the one at 870 nm for the π-polaron transitions.[12] Hence, UV-visible spectra of PANI and the composites confirm the availability of mixed states which is the prime requisite to make PANI conducting. The presence of polaron bands confirm the presence of polaron quasi particles, which plays an important role in charge transport through the composites.[45-46]

I-V characteristics:

The room-temperature I-V characteristics of the pelletized samples of PANI and the composites are shown in the Figure 3. All the I-V curves are non-linear, have saddle points at $V=0$ and are nearly symmetric about the origin. The current corresponding to any bias increases with increasing concentration of NGQDs. In fact, the maximum current (I_{max}) at 10 V is found to vary almost linearly with NGQD concentration [top right inset, Figure 3]. I_{max} through pelletized PANI is 0.6 mA, which increases to 13 mA following the addition of 10% NGQD, indicating a 22 times enhancement. The dynamic conductivity on the other hand increases super-linearly with the increase of NGQD concentrations [top left inset, Figure 3]. The maximum conductivity (at 10 V) of bare PANI sample was measured to be 0.05 S/m, which increased to 2.5 S/m with the addition of 10% NGQD, implying a 50 times enhancement of conductivity following NGQD incorporation at 10 V and at 300 K. The nearly symmetric nature of the I-V curves is apparent from the $\log I$ versus V curves shown as bottom right inset. Additionally, all the I-V curves exhibit hysteresis – a phenomenon that has immense potential application in novel memory devices.[47] We will not consider the hysteretic character further in this communication as it warrants a separate investigation.

Protonation of PANI (conversion of emeraldine base to emeraldine salt) is expected to produce a metallic state with no change in the number of electrons.[6] However, purely metallic conduction in PANI is seldom observed.[48] Even in highly conducting PANI charge transport is usually described by models describing disordered metals near metal-insulator transition

13

involving polaronic/bipolaronic conduction.[49] For our samples, spectroscopic signatures have suggested coupling of the π-electron of NGQDs with the electron lone pair in PANI and we have noted that incorporation of NGQD enhances the polaronic absorption peaks. As a result of this coupling of delocalized π-electrons of NGQDs with polarons in PANI, free holes are created in the N atoms of PANI network. It is well-known that conduction through PANI network is dictated by such p-type polaronic defect states.[50-51] The incorporation of NGQDs therefore, effectively behaves as free carrier injection resulting in consistent increase of conductivity with NGQD concentration. We have also seen that incorporation of NGQDs affect a quasi-alignment of the PANI rods resulting in an interconnected network structure. Since the polaronic conduction through a PANI network involves rearrangements of bonds, this alignment is expected to provide a greater length to polarons and bipolarons for hopping or translation along the polymer backbone interwind by the NGQDs. The super-linear increase of conductivity with NGQD doping concentration is therefore governed by a convoluted contribution of enhanced polaronic contribution due to effective charge injection and quasi alignment of the PANI backbone. However, at this stage it is not possible to decouple the individual contribution of enhanced electron-polaron coupling and alignment of PANI rods towards the observed increase in conduction. It is clear that such a decoupling would require a microscopic mechanism that should take into account both geometrical modification of the polymer structure and appearance of polaronic and/or bipolaronic states in the gap driven by such geometrical changes upon doping. These states could be detected and quantified by well-established electron spin resonance,[52] or optical methods,[53] which provide a good statistics of polarons and bipolarons in PANI.[54-56] Nonetheless, as we have discussed, from the UV-visible and FTIR spectra, we could qualitatively comment on the enhancement of intensity of the polaronic bands which supports active polaronic contribution due to NGQD doping. Furthermore, a close examination of the FTIR spectra in Fig. 2b shows the intensity of the peak

at 1110 cm^{-1} for doped PANI which measures the degree of delocalization of the electrons, increases for the NGQD–PANI composites. This increase in intensity is related to the increase in polaron density.[57-58] Furthermore, the peaks are slightly red-shifted with increase of NGQD which signifies an interaction between the π-bonded structure of NGQDs and the conjugated structure of PANI.[59-60] This certainly does not rule out conductivity enhancement arising from alignment of PANI rods but without specific quantitative measurements, it is difficult to comment on the relative contributions.
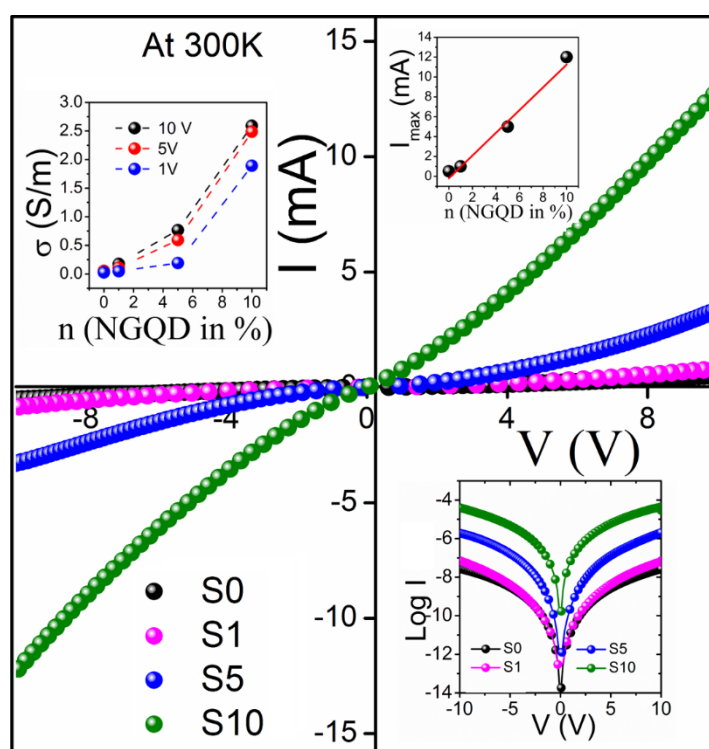

Figure 3. Room-temperature *I-V* characteristics of pelletized PANI and NGQD-PANI composites. The top left inset shows the variation of conductivity with respect to NGQD concentration at room temperature for 3 different bias voltages. The top right inset shows the near linear variation of maximum current density (I_{max} at 10 V) with respect to NGQD concentration. The variation of $\log I$ versus *V* is shown as the bottom right inset.

From the preceding discussions it is clear that although explaining the precise mechanism of conductivity enhancement involves understanding the microscopic picture, mechanism of charge transfer can be independently elucidated. To proceed, we measure the temperature-dependent I-V characteristics which allows us to examine various transport modes in the system. Representative temperature-dependent I-V characteristics of samples S0 (PANI) and S10 (PANI + 10% NGQD) are shown in Figure 4a and b respectively. The full set of I-V curves for all the samples are given in the supporting information, Figure S3. Within the measured temperature range, we do not notice any discernible change in the nature of the I-V curves with respect to the room temperature features — all the curves are non-linear, symmetric about V=0, exhibit hysteresis and have saddle points about V=0. For all samples, the current consistently decreases with decrease in temperature and this trend appears similar in all the samples. Figure 4c shows the temperature dependent conductivities at three different bias voltages (1, 5 and 10 V) for all the four samples – S0, S1, S5 and S10. The conductivity of all the samples increases exponentially with increase in temperature and for a given sample, it decreases with decreasing voltage at a given temperature. The exponential increase in conductivity with temperature is commensurate with the exponential increase in the charge carriers due to breaking of the benzenoid to quinoid units. [61-63] For all temperatures and bias voltages the conductivity of the samples continues to exhibit the same super-linear variation with NGQD concentration as observed in room temperature (supporting information, Figure S4). We have also plotted the I-V data in a semi-log, log-log scale and the plots for different temperatures. However, in case of PANI-NGQD composites we do not observe any switching transitions or 'gap' voltage for the temperature range (down to 157 K) investigated here, as demonstrated in other reports.[64-65] To illustrate this point, we have included the semi-log and log-log plots in the supporting information (Supporting information, Figure S5).
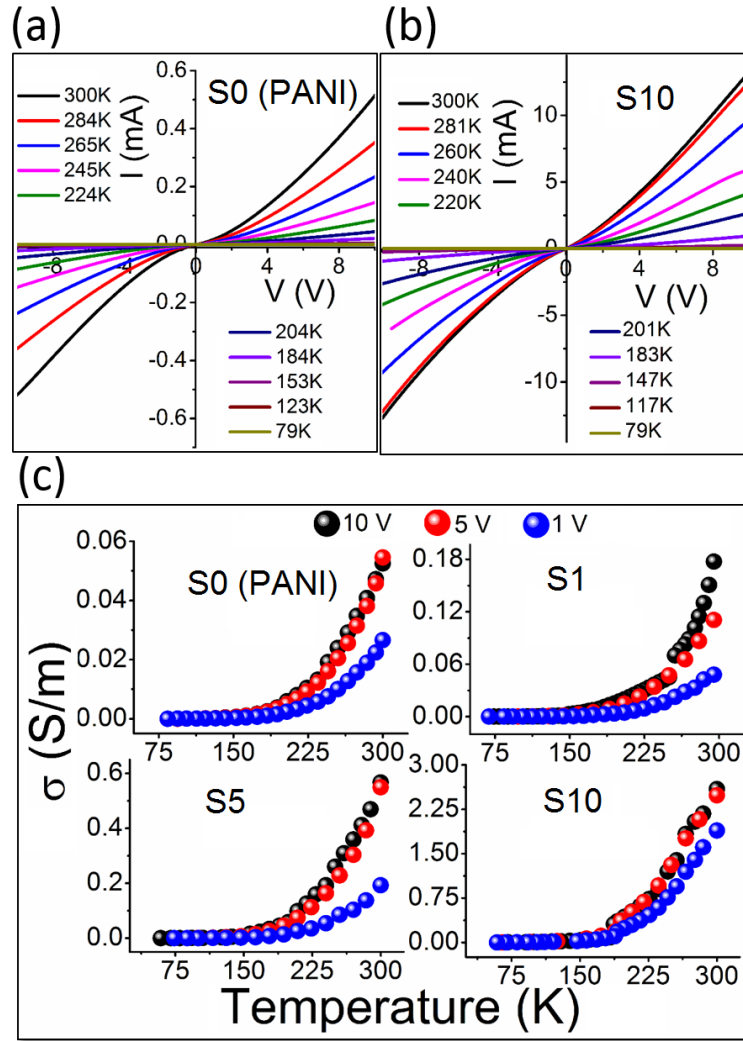
Figure 4. Temperature dependent *I-V* and conductivity. Representative temperature dependent *I-V* curves of (a) pelletized PANI and (b) 10% NGQD + PANI. (c) Variation of electrical conductivity (σ) with temperature of the samples at three different bias voltages: 1, 5 and 10 V.

The variation of dynamic conductance (*G*) with 1000/*T,* for bias voltages 1, 5 and 10 V, respectively, are plotted in Figure 5. Interestingly, we see that each plot is segmented into 3 or 4 continuous curves separated by discontinuities. The three continuous segments in the graphs corresponding to 5 and 10 V bias are marked by regions I, II and III. For 1 V bias we see that an additional region IV appears at lower temperatures. These three/four regions become more demarcated with the addition of NGQD in PANI. The presence of distinctly different regions

separated by discontinuities, dependent on the NGQD concentration and bias voltage, indicate towards different dominant mechanisms of charge transport operative in each region. We label the transition temperatures as 'crossover temperatures' since they mark the crossover from one mechanism to another. From Table 1 it is clear that the crossover temperatures from region I to II, followed by region II to III, and from region III to IV consistently decrease with increase in NGQD content and with increase in bias voltage.
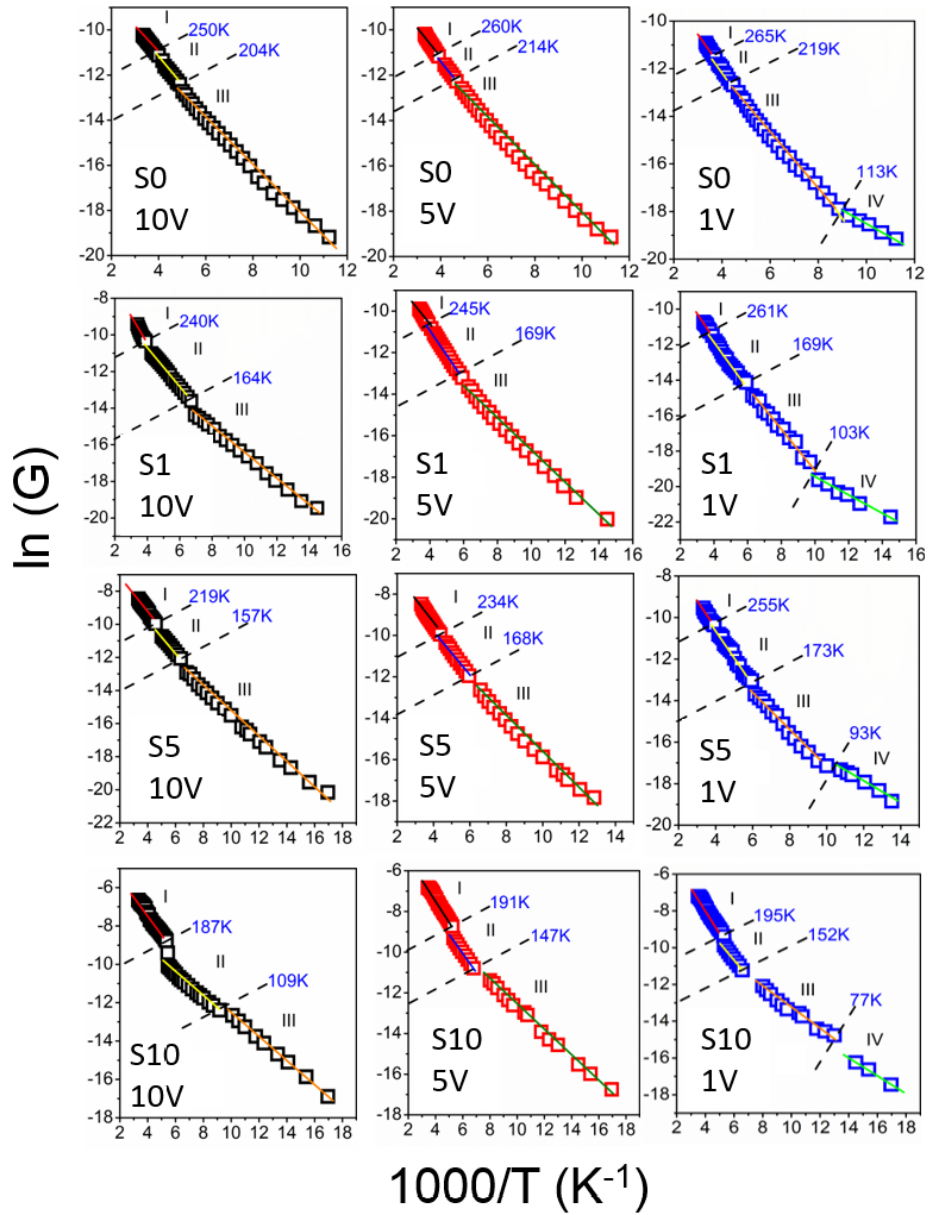
Figure 5. Variation of conductance (G) versus $1000/T$ plotted in the log scale for PANI, S1, S5 and S10, corresponding to 3 different bias voltages 1, 5 and 10 V. The graphs for 10 and 5 V, consist of three distinctly demarcated regions, whereas, the graphs for 1 V consist of 4 different regions. The regions are marked and the temperatures for crossover from one region to the other are indicated.

Table 1: Crossover temperatures corresponding to transition from one region to another as a function of bias voltage and sample

Samples	Bias Voltage (V)	Crossover temperature (K)		
		I – II	II – III	III – IV
PANI	10	250	204	-
	5	260	214	-
	1	265	219	113
S1	10	240	164	-
	5	245	169	-
	1	261	169	103
S5	10	219	157	-
	5	234	168	-
	1	255	173	93
S10	10	187	109	-
	5	191	147	-
	1	195	152	77

Following Figure 5, we investigated each region I, II, III and IV, separately. In region I, i.e. the high temperature region, for each sample and for all the three bias voltages, the dominant

mechanism for electrical transport is found to follow simple thermally activated conduction obeying Arrhenius law:

$$G(T) = G_{o} \exp\left(-\frac{E_a}{k_B T}\right) \qquad (1)$$

where, E_a is the activation energy, k_B is the Boltzmann constant, G is the conductance corresponding to the bias voltage and G_o is the pre-factor. In the mid temperature regime (region II), we observe a deviation from Arrhenius law for all the cases and the transport is dominated by thermally activated hopping. We fit our data using the well-known Larkin and Khmelnitskii (L-K) model of activation conduction in disordered systems.[22]

$$G(T) \propto \exp\left[-\frac{E_{a1}}{k_B T} \ln(\alpha T - \beta)\right] \qquad (2)$$

where, E_{a1} is the reduced activation energy, α and β are the parameters that depend on the localization length, hopping length, electric field, and pellet thickness.[66] The excellent fit in this region demonstrates the agreement with this model and the corresponding reduced activation energy values estimated in Table 2 are in good agreement with previous reports on transport in disordered structures through thermally activated hopping.[67]

In the region III (lower temperature regime), the conduction model for all samples deviate from the L-K equation as sufficient thermal activation for hoping is not available at low temperatures. The temperature below which thermally activated hopping is not possible, marks the crossover from region II to III wherein, variable range hopping (VRH) becomes the dominant transport mechanism. In this region and for the given temperature range, both Efros-Shklovskii variable range hopping (ES-VRH) and standard 3D VRH models produce nearly identical fits with the experimental data. However, we believe that ES-VRH given by equation (3),[68] better describes the system since the dimensionality of charge transport in the L-K model

20

varies from 0.85 to 1.6 (discussed later) for pristine and doped samples, respectively. Also, the fit of experimental data with equation (3) is marginally better that the fit with standard 3D VRH model (See supporting information, Figure S6 for details):

$$G(T) = G_o \exp\left(-\frac{T_o}{T}\right)^{1/2} \tag{3}$$

where, T_o is a material dependent constant and G_o is the pre-factor.

When the temperature and bias are both sufficiently low (region IV), the material as a whole behaves almost like an insulator as the conductivity values drop below 10^{-5} S/m. For the samples under investigation, this region appears only when the bias voltage is 1 V or less. This region can extend to higher voltages at sufficiently low temperatures where the associated thermal energies would be even lower. The transition temperatures and the maximum conductivities in this region are given in Table S2. As expected, the presence of NGQDs lowers the temperature of crossover to region IV by effectively injecting more carriers at a fixed temperature.

To further elucidate on the transport features, we calculated the representative transport parameters governing charge conduction in the three different regions, for 10 V bias. It is reasonable to assume that the basic mechanistic description of the three conducting regions will remain same for the other bias regimes albeit with different temperature bounds. Arrhenius activation energy (E_a) for region I, reduced activation energy (E_{a1}) and dimensionality (d) of charge transport for region II, and the material dependent transport parameter (T_o) describing the ES-VRH operative in region III, were estimated from the $\ln G$ versus $1/T$, $\log W$ versus $\log T$ and $\ln G$ versus $1/\sqrt{T}$ plots, respectively, and are presented in Table 2. For details, see Figure S7 supporting information. As expected, the activation energies (E_a and E_{a1}) decrease consistently with increase in NGQDs due to the effective increase in polaronic charge carriers.

The dimensionality of charge transport, d is found to vary from 0.85 in PANI to 1.6 in sample S10, consistent with the evolution of the sample morphology from disordered agglomerated lumps to an interconnected quasi 2D network. The estimated T_o values for ES-VRH are also in excellent agreement with the reported values.[69-70] The remarkable fit of the transport models with the experimental data, agreement of the extracted transport parameters with previous reports and consistency with structural features strongly establish that three different mechanisms of charge transport are operative in three different temperature regions for the NGQD-PANI nanocomposites.

Table 2. Transport parameters estimated from different models:

Transport Parameters	PANI	S1	S5	S10
E_a (meV)	98±1.61	80±1.80	77±1.68	67±2.43
E_{a1} (meV)	18±0.088	12±0.089	10.8±0.089	6.8±0.087
T_o (K)	$3.5*10^4$	$2.7*10^4$	$2.7*10^4$	$1.9*10^4$
d (for L-K transport)	0.85	~ 1	1	1.6
σ S/m (300 K)	0.05248	0.17747	0.56654	2.59078

Conclusions

In summary, we have performed a comprehensive study of charge transport in NGQD-dispersed conducting PANI matrix nanocomposites as a function of temperature, doping and

voltage bias. Importantly, while the NGQD doping dependence of conductivity can be simply explained by increased electron-polaron coupling, the conductivity variation with temperature shows a rich and complex behaviour resulting from an interplay of thermal and electron localization effects with clearly marked transitions between these behaviours. Perhaps equally as importantly, we show that this transition can be tuned by doping and voltage bias offering key insights into the underlying conduction mechanisms and pathways to tune conductivities. Our study not only is fundamentally interesting to understand conductivity mechanisms in disordered composite systems, but can potentially inform design strategies of future devices using similar materials.

Author Information

Corresponding Author

*Email: mallar.ray@tec.mx

ORCHID: 0000-0001-8173-1857

Supporting Information

Supporting Information is available online at www.pubs.acs.org

References

(1) Kurzmann, A.; Eich, M.; Overweg, H.; Mangold, M.; Herman, F.; Rickhaus, P.; Pisoni, R.; Lee, Y.; Garreis, R.; Tong, C. Excited states in bilayer graphene quantum dots. *Physical review letters* **2019,** *123* (2), 026803.

(2) Dirks, T.; Hughes, T. L.; Lal, S.; Uchoa, B.; Chen, Y.-F.; Chialvo, C.; Goldbart, P. M.; Mason, N. Transport through Andreev bound states in a graphene quantum dot. *Nature Physics* **2011,** *7* (5), 386-390.

(3) Ponomarenko, L. A.; Schedin, F.; Katsnelson, M. I.; Yang, R.; Hill, E. W.; Novoselov, K. S.; Geim, A. K. Chaotic Dirac billiard in graphene quantum dots. *Science* **2008,** *320* (5874), 356-358.

(4) Joung, D.; Zhai, L.; Khondaker, S. I. Coulomb blockade and hopping conduction in graphene quantum dots array. *Physical Review B* **2011,** *83* (11), 115323.

(5) Dresselhaus, M. S.; Chen, G.; Tang, M. Y.; Yang, R.; Lee, H.; Wang, D.; Ren, Z.; Fleurial, J. P.; Gogna, P. New directions for low-dimensional thermoelectric materials. *Advanced materials* **2007,** *19* (8), 1043-1053.

(6) Heeger, A. The fourth generation of semiconducting and metallic polymers: Nobel Lecture: polymeric materials. *Reviews of Modern Physics* **2001,** *73*, 681-700.

(7) MacDiarmid, A. G.; Epstein, A. J. Polyanilines: a novel class of conducting polymers. *Faraday Discussions of the Chemical Society* **1989,** *88*, 317-332.

(8) Ramachandran, A.; JS, A. N.; Karunakaran Yesodha, S. Polyaniline-derived nitrogen-doped graphene quantum dots for the ultratrace level electrochemical detection of trinitrophenol and the effective differentiation of nitroaromatics: structure matters. *ACS Sustainable Chemistry & Engineering* **2019,** *7* (7), 6732-6743.

(9) Hakimi, M.; Salehi, A.; Boroumand, F.; Mosleh, N. Fabrication of a room temperature ammonia gas sensor based on polyaniline with N-doped graphene quantum dots. *IEEE Sensors Journal* **2018,** *18* (6), 2245-2252.

(10) Gebreegziabher, G. G.; Asemahegne, A. S.; Ayele, D. W.; Mani, D.; Narzary, R.; Sahu, P. P.; Kumar, A. Polyaniline–graphene quantum dots (PANI–GQDs) hybrid for plastic solar cell. *Carbon Letters* **2020,** *30* (1), 1-11.

(11) Lai, S. K.; Luk, C. M.; Tang, L.; Teng, K. S.; Lau, S. P. Photoresponse of polyaniline-functionalized graphene quantum dots. *Nanoscale* **2015,** *7* (12), 5338-5343.

(12) Maity, N.; Kuila, A.; Das, S.; Mandal, D.; Shit, A.; Nandi, A. K. Optoelectronic and photovoltaic properties of graphene quantum dot–polyaniline nanostructures. *Journal of Materials Chemistry A* **2015,** *3* (41), 20736-20748.

(13) Huang, Z.; Li, L.; Wang, Y.; Zhang, C.; Liu, T. Polyaniline/graphene nanocomposites towards high-performance supercapacitors: a review. *Composites Communications* **2018,** *8*, 83-91.

(14) Bak, S.; Kim, D.; Lee, H. Graphene quantum dots and their possible energy applications: A review. *Current Applied Physics* **2016,** *16* (9), 1192-1201.

(15) Zhao-bin, S.; Lu, Y. Soliton and polaron dynamics in conducting polymers. *Physica Scripta* **1987,** *1987* (T19A), 231.

(16) Bredas, J. L.; Street, G. B. Polarons, bipolarons, and solitons in conducting polymers. *Accounts of Chemical Research* **1985,** *18* (10), 309-315.

(17) Su, W. P.; Schrieffer, J.; Heeger, A. J. Solitons in polyacetylene. *Physical review letters* **1979,** *42* (25), 1698.

(18) Syed, A. A.; Dinesan, M. K. Polyaniline—A novel polymeric material. *Talanta* **1991,** *38* (8), 815-837.

(19) Luk, C.; Chen, B.; Teng, K.; Tang, L.; Lau, S. Optically and electrically tunable graphene quantum dot–polyaniline composite films. *Journal of Materials Chemistry C* **2014,** *2* (23), 4526-4532.

(20) Kalita, H.; Shinde, D. B.; Pillai, V. K.; Aslam, M. Hysteresis and charge trapping in graphene quantum dots. *Applied Physics Letters* **2013,** *102* (14), 143104.

(21) Nieves, C. A.; Martinez, L. M.; Melendez, A.; Ortiz, M.; Ramos, I.; Pinto, N. J.; Zimbovskaya, N. Temperature-dependent charge transport mechanisms in carbon sphere/polyaniline composite. *AIP Advances* **2017,** *7* (12), 125229.

(22) Mombrú, D.; Romero, M.; Faccio, R.; Mombrú, A. l. W. Tuning electrical transport mechanism of polyaniline–graphene oxide quantum dots nanocomposites for potential electronic device applications. *The Journal of Physical Chemistry C* **2016,** *120* (43), 25117-25123.

(23) Bhattacharjee, L.; Manoharan, R.; Mohanta, K.; Bhattacharjee, R. R. Conducting carbon quantum dots–a nascent nanomaterial. *Journal of Materials Chemistry A* **2015,** *3* (4), 1580-1586.

(24) Zhang, L. L.; Zhao, X.; Ji, H.; Stoller, M. D.; Lai, L.; Murali, S.; Mcdonnell, S.; Cleveger, B.; Wallace, R. M.; Ruoff, R. S. Nitrogen doping of graphene and its effect on quantum capacitance, and a new insight on the enhanced capacitance of N-doped carbon. *Energy & Environmental Science* **2012,** *5* (11), 9618-9625.

(25) Miah, M.; Bhattacharya, S.; Gupta, A.; Saha, S. K. Origin of high storage capacity in N-doped graphene quantum dots. *Electrochimica Acta* **2016,** *222*, 709-716.

(26) Gan, X.; Yang, S.; Zhang, J.; Wang, G.; He, P.; Sun, H.; Yuan, H.; Yu, L.; Ding, G.; Zhu, Y. Graphite-N Doped Graphene Quantum Dots as Semiconductor Additive in Perovskite Solar Cells. *ACS applied materials & interfaces* **2019,** *11* (41), 37796-37803.

(27) Qu, D.; Zheng, M.; Zhang, L.; Zhao, H.; Xie, Z.; Jing, X.; Haddad, R. E.; Fan, H.; Sun, Z. Formation mechanism and optimization of highly luminescent N-doped graphene quantum dots. *Scientific reports* **2014,** *4*, 5294.

(28) Wei, Y.; Tang, X.; Sun, Y.; Focke, W. W. A study of the mechanism of aniline polymerization. *Journal of Polymer Science Part A: Polymer Chemistry* **1989,** *27* (7), 2385-2396.

(29) Tang, L.; Ji, R.; Li, X.; Bai, G.; Liu, C. P.; Hao, J.; Lin, J.; Jiang, H.; Teng, K. S.; Yang, Z. Deep ultraviolet to near-infrared emission and photoresponse in layered N-doped graphene quantum dots. *ACS nano* **2014,** *8* (6), 6312-6320.

(30) Permatasari, F. A.; Aimon, A. H.; Iskandar, F.; Ogi, T.; Okuyama, K. Role of C–N configurations in the photoluminescence of graphene quantum dots synthesized by a hydrothermal route. *Scientific reports* **2016,** *6*, 21042.

(31) Eberlein, T.; Bangert, U.; Nair, R.; Jones, R.; Gass, M.; Bleloch, A.; Novoselov, K.; Geim, A.; Briddon, P. Plasmon spectroscopy of free-standing graphene films. *Physical Review B* **2008,** *77* (23), 233406.

(32) Zhang, Y.; Duan, Y.; Liu, J.; Ma, G.; Huang, M. Wormlike acid-doped polyaniline: controllable electrical properties and theoretical investigation. *The Journal of Physical Chemistry C* **2018,** *122* (4), 2032-2040.

(33) Devadas, B.; Imae, T. Effect of carbon dots on conducting polymers for energy storage applications. *ACS Sustainable Chemistry & Engineering* **2018,** *6* (1), 127-134.

(34) Zhang, H.; Chen, Y.; Liang, M.; Xu, L.; Qi, S.; Chen, H.; Chen, X. Solid-phase synthesis of highly fluorescent nitrogen-doped carbon dots for sensitive and selective probing ferric ions in living cells. *Analytical chemistry* **2014,** *86* (19), 9846-9852.

(35) Qu, D.; Zheng, M.; Du, P.; Zhou, Y.; Zhang, L.; Li, D.; Tan, H.; Zhao, Z.; Xie, Z.; Sun, Z. Highly luminescent S, N co-doped graphene quantum dots with broad visible absorption bands for visible light photocatalysts. *Nanoscale* **2013,** *5* (24), 12272-12277.

(36) Palaniappan, S.; Nivasu, V. Emulsion polymerization pathway for preparation of organically soluble polyaniline sulfate. *New Journal of Chemistry* **2002,** *26* (10), 1490-1494.

(37) Bhandari, S. Polyaniline: Structure and Properties Relationship. In *Polyaniline Blends, Composites, and Nanocomposites*; Elsevier: 2018; pp 23-60.

(38) Saikia, A.; Karak, N. Polyaniline nanofiber/carbon dot nanohybrid as an efficient fluorimetric sensor for As (III) in water and effective antioxidant. *Materials Today Communications* **2018,** *14*, 82-89.

(39) Chhabra, V. A.; Kaur, R.; Walia, M. S.; Kim, K.-H.; Deep, A. PANI/PbS QD nanocomposite structure for visible light driven photocatalytic degradation of rhodamine 6G. *Environmental Research* **2020**, 109615.

(40) Kundu, A.; Shit, A.; Nandi, S. Carbon dot assisted synthesis of nanostructured polyaniline for dye sensitized solar cells. *Energy & fuels* **2017,** *31* (7), 7364-7371.

(41) Raut, B.; Chougule, M.; Nalage, S.; Dalavi, D.; Mali, S.; Patil, P.; Patil, V. CSA doped polyaniline/CdS organic–inorganic nanohybrid: physical and gas sensing properties. *Ceramics International* **2012,** *38* (7), 5501-5506.

(42) Huang, W.; MacDiarmid, A. Optical properties of polyaniline. *Polymer* **1993,** *34* (9), 1833-1845.

(43) Yang, C.; Fang, Z.; Zhang, P. UV-Vis spectra of polyaniline doped with camphor sulfonic acid in different organic solvents. *Journal of Central South University of Technology* **1999,** *6* (2), 127-129.

(44) Scotto, J.; Florit, M. I.; Posadas, D. About the species formed during the electrochemical half oxidation of polyaniline: Polaron-bipolaron equilibrium. *Electrochimica Acta* **2018,** *268*, 187-194.

(45) Adhikari, S.; Banerji, P. Enhanced conductivity in iodine doped polyaniline thin film formed by thermal evaporation. *Thin Solid Films* **2010,** *518* (19), 5421-5425.

(46) Thiyagarajan, M.; Samuelson, L. A.; Kumar, J.; Cholli, A. L. Helical conformational specificity of enzymatically synthesized water-soluble conducting polyaniline nanocomposites. *Journal of the American Chemical Society* **2003,** *125* (38), 11502-11503.

(47) Xu, Z.; Liu, Z.; Huang, Y.; Zheng, G.; Chen, Q.; Zhou, H. To probe the performance of perovskite memory devices: defects property and hysteresis. *Journal of Materials Chemistry C* **2017,** *5* (23), 5810-5817.

(48) Lee, K.; Cho, S.; Park, S. H.; Heeger, A.; Lee, C.-W.; Lee, S.-H. Metallic transport in polyaniline. *Nature* **2006,** *441* (7089), 65-68.

(49) Heeger, A. J. The critical regime of the metal-insulator transition in conducting polymers: experimental studies. *Physica Scripta* **2002,** *2002* (T102), 30.

(50) Bartonek, M.; Kuzmany, H. Resonance Raman scattering from the polaron state in polyaniline. *Synthetic metals* **1991,** *41* (1-2), 607-612.

(51) McCall, R.; Ginder, J.; Leng, J.; Ye, H.; Manohar, S.; Masters, J.; Asturias, G.; MacDiarmid, A.; Epstein, A. Spectroscopy and defect states in polyaniline. *Physical Review B* **1990,** *41* (8), 5202.

(52) Scott, J.; Pfluger, P.; Krounbi, M.; Street, G. Electron-spin-resonance studies of pyrrole polymers: Evidence for bipolarons. *Physical Review B* **1983,** *28* (4), 2140.

(53) Brédas, J.-L.; Scott, J.; Yakushi, K.; Street, G. Polarons and bipolarons in polypyrrole: Evolution of the band structure and optical spectrum upon doing. *Physical Review B* **1984,** *30* (2), 1023.

(54) Chen, J.; Heeger, A.; Wudl, F. Confined soliton pairs (bipolarons) in polythiophene: In-situ magnetic resonance measurements. *Solid state communications* **1986,** *58* (4), 251-257.

(55) Nechtschein, M.; Devreux, F.; Genoud, F.; Vieil, E.; Pernaut, J.; Genies, E. Polarons, bipolarons and charge interactions in polypyrrole: physical and electrochemical approaches. *Synthetic metals* **1986,** *15* (1), 59-78.

(56) Zotti, G.; Schiavon, G. Spectroclectrochemical determination of polarons in polypyrrole and polyaniline. *Synthetic metals* **1989,** *30* (2), 151-158.

(57) Kellenberger, A.; Dmitrieva, E.; Dunsch, L. Structure dependence of charged states in "linear" polyaniline as studied by in situ ATR-FTIR spectroelectrochemistry. *The Journal of Physical Chemistry B* **2012,** *116* (14), 4377-4385.

(58) Kazim, S.; Ali, V.; Zulfequar, M.; Haq, M. M.; Husain, M. Electrical, thermal and spectroscopic studies of Te doped polyaniline. *Current Applied Physics* **2007,** *7* (1), 68-75.

(59) Mitra, M.; Kulsi, C.; Chatterjee, K.; Kargupta, K.; Ganguly, S.; Banerjee, D.; Goswami, S. Reduced graphene oxide-polyaniline composites—synthesis, characterization and optimization for thermoelectric applications. *RSC Advances* **2015,** *5* (39), 31039-31048.

(60) Quillard, S.; Louarn, G.; Lefrant, S.; MacDiarmid, A. Vibrational analysis of polyaniline: a comparative study of leucoemeraldine, emeraldine, and pernigraniline bases. *Physical Review B* **1994,** *50* (17), 12496.

(61) de Oliveira Jr, Z.; Dos Santos, M. Relative stability of polarons and bipolarons in emeraldine oligomers: a quantum chemical study. *Solid state communications* **2000,** *114* (1), 49-53.

(62) Le, T.-H.; Kim, Y.; Yoon, H. Electrical and electrochemical properties of conducting polymers. *Polymers* **2017,** *9* (4), 150.

(63) Mu, S.; Kan, J.; Lu, J.; Zhuang, L. Interconversion of polarons and bipolarons of polyaniline during the electrochemical polymerization of aniline. *Journal of Electroanalytical Chemistry* **1998,** *446* (1-2), 107-112.

(64) Rahman, A.; Sanyal, M. K. Correlated Charge Carrier-like Photoresponse of Polymer Nanowires. *ACS nano* **2013,** *7* (9), 7894-7900.

(65) Rahman, A.; Sanyal, M. K. Observation of charge density wave characteristics in conducting polymer nanowires: Possibility of Wigner crystallization. *Physical Review B* **2007,** *76* (4), 045110.

(66) Larkin, A.; Khmel'nitskii, D. Activation conductivity in disordered systems with large localization length. *Sov. Phys. JETP* **1982,** *56* (3), 647.

(67) Mombrú, D.; Romero, M.; Faccio, R.; Mombrú, Á. W. Effect of graphene-oxide on the microstructure and charge carrier transport of polyaniline nanocomposites under low applied electric fields. *Journal of Applied Physics* **2017,** *121* (4), 045109.

(68) Éfros, A. L.; Shklovskii, B. I. Coulomb gap and low temperature conductivity of disordered systems. *Journal of Physics C: Solid State Physics* **1975,** *8* (4), L49.

(69) Kobayashi, A.; Xu, X.; Ishikawa, H.; Satoh, M.; Hasegawa, E. Electrical conduction in polyaniline compressed pellets doped with alkylbenzenesulfonic acids. *Journal of applied physics* **1992,** *72* (12), 5702-5705.

(70) Lin, Y.-F.; Chen, C.-H.; Xie, W.-J.; Yang, S.-H.; Hsu, C.-S.; Lin, M.-T.; Jian, W.-B. Nano approach investigation of the conduction mechanism in polyaniline nanofibers. *Acs Nano* **2011,** *5* (2), 1541-1548.

TOC graphic